Kriging Assisted Integrated Rotor-Duct Optimization for Ducted Fan in Hover

Jixiang Qing* Hu Yu[†] Yanling Wang[‡] Zhonghuan Liu[§] Xuyang Fu[¶] School of Aeronautics, Northwestern Polytechnical University, Xian, Shannxi, 710072

Wenmeng Liu[∥]

School of Electronical and Computer Engineering, University of Victoria 3800 Finnerty Rd, Victorial, BC, V8P 5CS

The design of ducted fan was primarily based on parametric analysis and the existing optimization design studies mainly focus on either the rotor or the duct alone. However, the interactions between the rotor and duct remarkably affects the performance of the ducted fan. Therefore, it has been expected that an integrated optimization such the rotor-duct interactions are involved could result in a better design. In this paper, the integrated rotor-duct optimization was performed. Then it was compared with several different optimized configurations. The Reynolds-Averaged Navier-Stokes solver incorporated with momentum source method was adopted to predict performance of ducted fan and it was validated by force measurement experiments. The duct shape was parameterized by the FFD method and the blade shape was modeled by Bezier splines. A surrogate based optimization framework using Kriging model was developed. The hovering efficiency was set as the objective function subjecting to the thrust constraint. The optima from different optimized configurations were analyzed with the help of crossover studies. The analysis revealed that the improvement of the ducted fan hovering efficiency is primarily restricted by the flow separations in the duct. When the shape of both the rotor and duct was involved into the design optimization, the blade with longer chord at blade tip was obtained. This helps injecting more momentum into the boundary layer of the duct and the flow separation can be suppressed. Therefore, the integrated rotor-duct optimization produces the duct with larger diffuser expansion angle and better hovering efficiency.

I. Nomenclature

A = duct throat cross-section area C_l = blade section lift coefficient

 c_1, c_2, c_3 = parameters of propeller chord length distributions

 C_d = blade section drag coefficient Cy = force coefficient in the y direction c = blade section chord length

C = duct length

D = diameter of the duct
DL = ducted fan disk loading

FM = General figure of merit of ducted fan

 N_p = number of propeller blades

n = total number of the momentum source elements

P = local pressure of the flowfield P_{prop} = power consumption from the rotor P_{∞} = far field pressure, 1.013×10^5 Pa

^{*}Graduate Student, School of Aeronautics, tsingjixiang@yahoo.com

[†]Associate Professor, School of Aeronautics, julius_hu@hotmail.com

[‡]Graduate Student, School of Aeronautics

[§]Graduate Student, School of Aeronautics

[¶]Graduate Student, School of Aeronautics

Graduate Student, School of Electronical and Computer Engineering, wenmengliu@uvic.ca

PL = ducted fan power loading

 $q_{a_{tip_{baseline}}}$ = axial dynamic pressure at propeller tip of the baseline ducted fan

r = radial location of the blade element $S_{M_X}, S_{M_Y}, S_{M_Z}$ = momentum source at corresponding axis

 T_{total} = total thrust of ducted fan T_{prop} = thrust produced by rotor T_{duct} = thrust produced by duct

 V_a = axial velocity

 $V_{a_{tip_{baseline}}}$ = axial velocity at propeller tip of the baseline ducted fan

v = blade section inflow velocity

 α = blade section effective angle of attack β = blade section induced angle of attack

 $\beta_1, \beta_2, \beta_3$ = parameters of propeller twist angle distributions

 θ = blade section twist angle

 ρ_{∞} = freestream density, 1.225 Kg/ m^3

 ρ = density of the flow

x = relative position of the blade element, $x = \frac{2r}{D}$

 ω = propeller angular velocity

II. Introduction

Distill shows growing interest on many applications, like MAV, flying cars, helicopters and Fan-in-wing configurations. Apart from the high efficiency, its other appealing advantages are noise reduction and improved safety. While brings with extra lift, the flow in the duct becomes very complex that many geometry parameters like duct shape, propeller tip clearance and propeller shape tend to affect the performance of the system.

In order to analyze the flow mechanism of ducted fan, Grunwald and Goodson [1] investigated how the distribution of aerodynamic loads on the fan and duct contributed to the overall aerodynamics of the configuration. They confirmed that the duct is the main source of normal force and pitching moment and roughly half of the thrust is provided by the duct in hover. Black, Wainauski and Rohrhach [2] examined performance of a shrouded propellers with an experimental approach. Forces and moments were measured by changing variables such as lip shape, chord, exit area ratio, propeller location within the shroud, vanes, propeller blade shape, number of blades and blade clearance. The results showed that diffuser expansion ratio is the most critical variable. The effects of blade twist angle on performance of a four-feet ducted fan at zero angle of attack was experimentally investigated by Mort [3]. Results showed that Figure of Merit (FM) decreased rapidly at large blade twist angles. Graf, Fleming and Ng [4] investigated the effects of duct leading edge geometry by using five different duct lip shapes. It was observed that the performance of the ducted fan with large leading edge radius was enhanced in static conditions. Yilmaz [5] investigated a 16-inch ducted propeller experimentally using five different duct shapes. It was showed that the duct thrust originated from the suction effect induced by the propeller in converging part (forebody) of the duct, and an optimization of inlet shape for all advance ratio range of the vehicle is essential for a better design.

Flow mechanism and geometric parameter analysis are also carried out with the help of various numerical simulation models. From early blade element theories to Reynolds-averaged Navier-Stokes equations (RANS). To improve performance of the ducted fan, Ahn and Lee [6] used a computational method based on Euler equations and actuator disk model. Geometrical design parameters were investigated, and it was revealed that diffuser expansion angle is a dominant duct parameter, and the blade design should be coupled for the optimization of a ducted fan system. Schaller [7] developed a ducted fan shape optimization procedure to maximize the thrust of a duct configuration. The unsteady laminar incompressible Navier-Stocks (N-S) equations was incorporated with the momentum source model (MSM). Duct shape was parameterized by Non-Uniform Rational B-Splines and a Genetic Algorithm (GA) optimizer was used to find the optimum. Finally, a superior duct shape was found.

In previous researches, the design of ducted fan was primarily based on parametric analysis and the existing optimization design studies mainly focus on either the rotor or the duct. However, the interactions between the rotor and duct remarkably affects the performance of the ducted fan. Therefore, it has been expected that an integrated optimization with the rotor-duct interactions involved could result in a better design.

In this study, an integrated optimization of propeller geometry and duct shape was carried out for better hovering performance. The numerical simulation was based on incompressible N-S equations and MSM. Experiments were conducted to validate the numerical simulation model. Optima were found with the help of Kriging Surrogate Based Optimization (SBO) method. Crossover studies of optimum ducts and propellers were then performed. It was expected that this work will provide further understanding of duct and fan interactions and lead to a better design of the ducted fan. While this research is mainly concerned with ducted fan hovering performance, the conclusions of this paper should also be applicable for duct configuration working horizontally with no inflow velocity.

The remains of this paper were arranged into five sections. A brief overview of methods used to perform the computation and optimization was described in section three. The validation of the computational methods was stated in section four. The optimization problem was formulated in section five. Optimum results were presented and analyzed with the help of crossover studies in section six. Followed by the conclusions in section seven.

III. Computation Method and Optimization Algorithm

A. Ducted fan modeling and flow governing equations

A variety of numerical methods have been used to model the rotor of ducted fan. However, as the flow mechanism of duct is very complex, many geometry characteristics, such as inlet radius, tip clearance, will strongly affect the flow through the ducted fan and consequently the performance of the ducted fan system [8]. Traditional methods like simple momentum balance methods have limited capability to model the wake, and the ducted fan's geometric characteristics cannot be properly represented in these methods [8]. Modern computational fluid dynamics (CFD) methods have eliminated most of the restrictions, hence many researches computational have been carried out and results matches well with experimental data [9, 10]. However, relatively higher computation resource is required.

In this study, the MSM developed by Rajagopalan [11] was used to model the propeller, the airfoil characteristics were calculated by XFOIL [12]. In the MSM, the propeller is modeled as a force added to the momentum equation where cells have a propeller element at a certain time [8]. As shown in Fig.1, given the local flow conditions, rotation speed and the airfoil lift and drag characteristics, the section inflow velocity and the angle of attack can be obtained. The forces acting as implicit sources in the momentum equations can then be derived. Since the governing equations in this approach could be solved without any more assumptions on propeller element location and wake structure, a more physical result could be obtained. Several numerical studies [8, 13] based on MSM has been conducted and the results are promising.

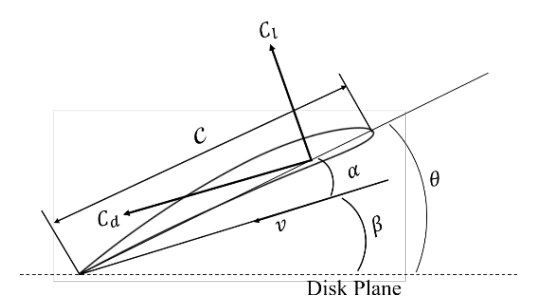


Fig. 1 Definitions of the parameters regarding the propeller section

The MSM neglected the flow around the blade surface, hence the effects of boundary layer separation could only be considered indirectly. However, no body-fitted grid and moving mesh techniques for the propeller are required. The number of mesh elements and computational costs can be significantly reduced in this way. Since the geometries of the propeller do not present in the mesh, no mesh morphing near the blade is required, this simplifies the optimization procedure and improves the robustness of the optimization.

In this paper, the steady incompressible N-S equations are used as the flow governing equations (Eq.1-Eq.4). The S_{M_x} , S_{M_y} , S_{M_z} are the momentum source terms at corresponding axis.

$$\frac{\partial u}{\partial x} + \frac{\partial v}{\partial y} + \frac{\partial w}{\partial z} = 0 \tag{1}$$

$$S_{M_x} - \frac{\partial p}{\partial x} + \mu \left(\frac{\partial^2 u}{\partial x^2} + \frac{\partial^2 u}{\partial y^2} + \frac{\partial^2 u}{\partial z^2}\right) = \rho \left(u\frac{\partial u}{\partial x} + v\frac{\partial u}{\partial y} + w\frac{\partial u}{\partial z}\right) \tag{2}$$

$$S_{M_{y}} - \frac{\partial p}{\partial y} + \mu \left(\frac{\partial^{2} v}{\partial x^{2}} + \frac{\partial^{2} v}{\partial y^{2}} + \frac{\partial^{2} v}{\partial z^{2}}\right) = \rho \left(u\frac{\partial v}{\partial x} + v\frac{\partial v}{\partial y} + w\frac{\partial v}{\partial z}\right)$$
(3)

$$S_{M_z} - \frac{\partial p}{\partial z} + \mu \left(\frac{\partial^2 w}{\partial x^2} + \frac{\partial^2 w}{\partial y^2} + \frac{\partial^2 w}{\partial z^2}\right) = \rho \left(u\frac{\partial w}{\partial x} + v\frac{\partial w}{\partial y} + w\frac{\partial w}{\partial z}\right) \tag{4}$$

A steady, incompressible CFD solver of the commercial software FLUENT 17.0 is adopted to solve the RANS governing equations. The momentum source is inserted to the flow by means of ANSYS Fluent User Defined Functions (UDF). The k-omega SST model is used as the turbulence model for its good behavior in adverse pressure gradients and separating flow. As the flow is incompressible, the pressure-based solver is used. The RANS governing equations are solved implicitly, and the SIMPLE algorithm is taken as the pressure-velocity coupling approach. The Green-Gauss node-based method is adopted in gradient interpolation. The convective flux terms and diffusive-flux terms are discretized with the second order-accurate upwind scheme and second-order-accurate central-difference scheme respectively.

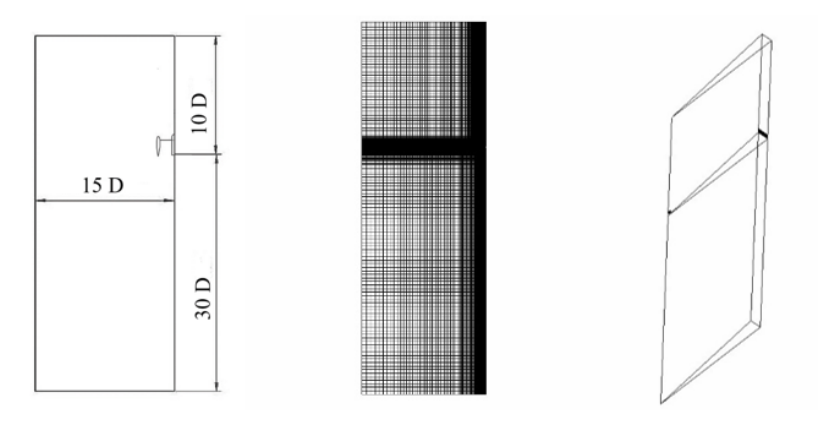


Fig. 2 Definition of the computation domain

The ducted fan is discretized by multi-block grid in a cylindrical region. In hovering condition, the flow is axis symmetric, therefore only a slice of the cylindrical region is meshed, as shown in Fig.2. On each side of the slice, the periodic boundary condition is specified. This approach decreases the total number of the grids hence is widely used in ducted fan analysis [9, 13]. Body fitted grids around the duct and center body are shown in Fig.3. The height of the first boundary layer mesh elements is set such that the y+ is equal to or less than 1. The total mesh element number is about 80,000.

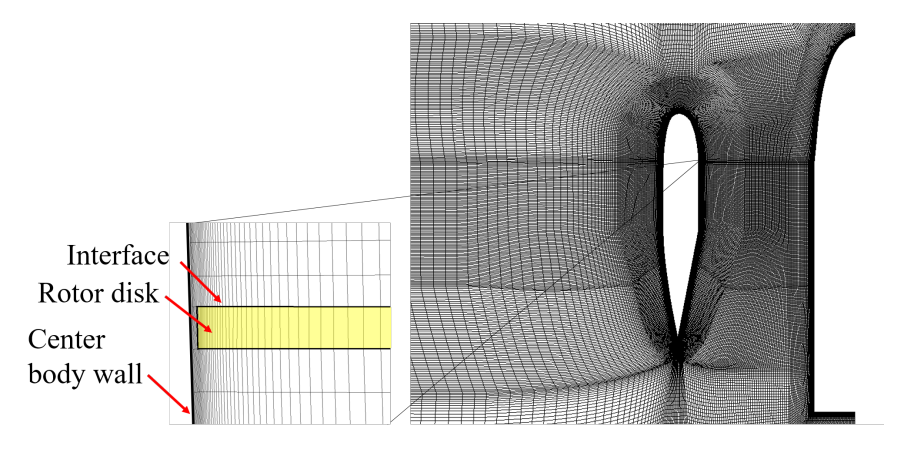


Fig. 3 Definition of the computation domain

B. Optimization algorithm

In this paper, the rotor shape, duct shape and integrated rotor-duct shape optimization were performed. The optimization results were then compared and studied. Gradient based optimizers, though converges fast and shows superiority for high dimension problems, often requires an initial design near the optimal and may struggle to find the global optimum [14]. For the integrated rotor-duct optimization, the gradient free algorithms (GFA) were preferred for insufficient knowledge about the optimum. However, traditional GFA like GA requires large amount of function calls. Due to large computational resources consumed by CFD methods, traditional GFAs will introduce very long computation time. The optimization based on direct function calls may even be impossible.

Therefore, the SBO method was employed. In this method, the surrogate model was built based on limited number of function calls. The sequential design strategies for global optimization was then performed so that the number of the expensive black box function calls can be reduced.

The surrogate models can be categorized into two types: the interpolate models and the regression models. The interpolate models creating best-fit response models [15], however, once the data set was noisy, overfit may occur. Regression models, though lacks certain accuracy on data, is more suitable in this circumstance instead. In this paper, the relative high fidelity computation method has been adopted so that the Kriging interpolating model was used for its capability of representing nonlinear and multidimensional functions. Moreover, this model has a unique feature of offering a mean-squared-error estimation [16]. A Latin hypercube sampling (LHS) [17] technique was used to provide the initial samples for surrogate model construction.

The expected improvement (EI) and minimize surrogate prediction (MSP) were employed as the infill criteria in sequential design process of this optimization. The combination of EI and MSP gives good compromise between exploitation and exploration of surrogate models. The GA was used by these two sub-optimizations. The SBO was carried out with the help of ooDACE toolbox [18].

C. Geometry parameterization

The free-form deformation (FFD) was used to morph the duct shape and adjust adjacent mesh elements. As presented in Fig.4, the duct shape and adjacent grids were parameterized in FFD volumes. The points on the boundary of FFD volume controls the deformation and thus can be used as design variables. In this study, 6 pairs of FFD control points were selected as design variables. Each pair has two corresponding control points on the periodic boundaries. These control points are able to handle the geometries of the duct such as inlet radius, diffuser length and expansion angle. More details of the design variables will be described in section four.

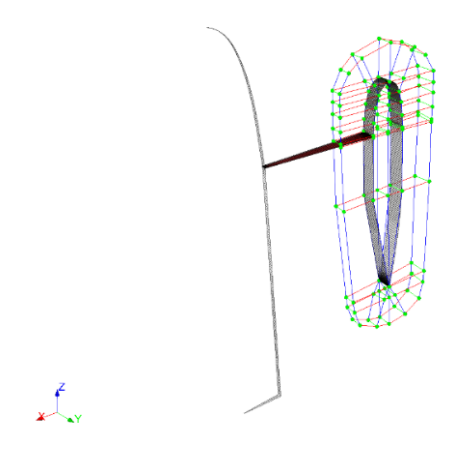


Fig. 4 FFD control volumes near the duct

The Bezier quadratic spline was used to parameterize propeller twist angle distribution and the chord distribution. There were 3 design variables for each spline, as shown in Eq.5 and Eq.6

$$c_p(x) = (1-x)^2 c_1 + 2x(1-x)c_2 + x^2 c_3$$
(5)

$$\beta_p(x) = (1 - x)^2 \beta_1 + 2x(1 - x)\beta_2 + x^2 \beta_3$$
 (6)

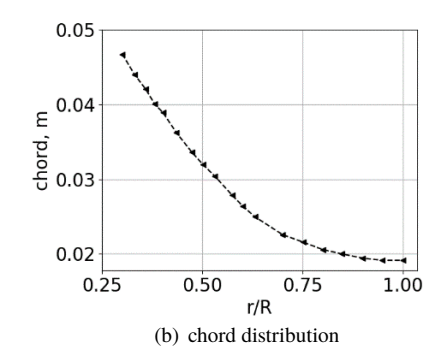
IV. Validation of the computation method

To validate the computation method, performance of the ducted fan defined in Tab.1 and Fig.5 at hovering condition was obtained by experiments. The duct shape was the same as the one proposed by Grunwald et al [1]. The three-bladed propeller geometry was illustrated in Fig.5, with the section airfoil of NACA 6412.

Table 1 Primary parameters of the experimental ducted fan

Parameters	Value
Disk diameter, mm	381
Blade number	3
Duct height, mm	262
Tip clearance, mm	1.5
Propeller Rotation speed, RPM	2000~8000
Propeller section airfoil	NACA 6412





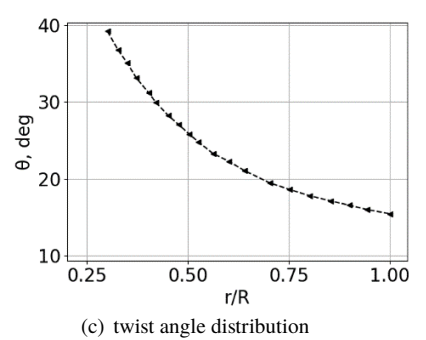


Fig. 5 Geometry of the experimental propeller

A. Experiment setup

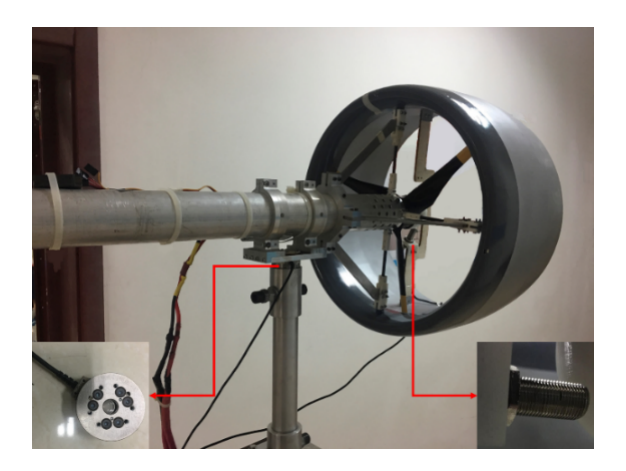


Fig. 6 Experimental model of the ducted fan

The experimental apparatus was shown in Fig.6 and the scheme for the experimental system was presented in Fig.7. The force and torque were measured by an ATI Mini45 force/torque sensor, which was powered by a high precision voltage supply with maximum error of 50 μ V. Hall effect tachometer was used to measure the rotation speed of the

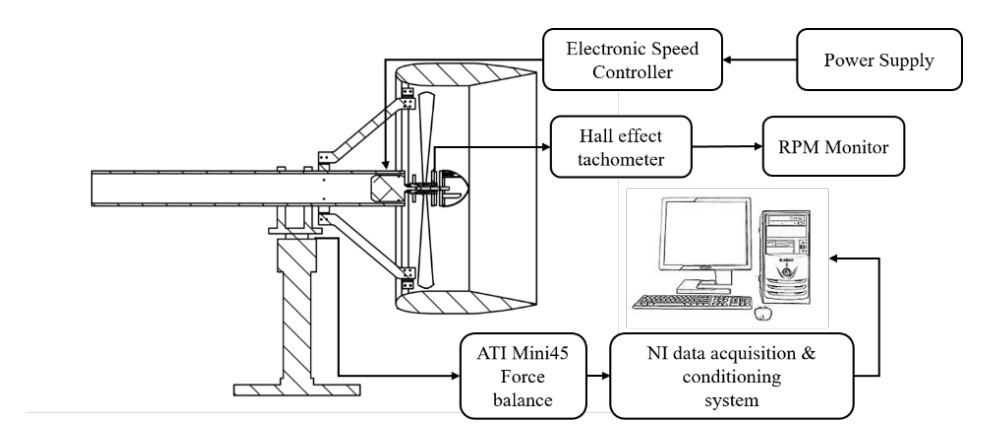


Fig. 7 The experiment setup of the ducted fan

propeller. The signal from ATI Mini45 was acquired and processed by the NI PCI-6133 and NI PXI 1520 card. The measurement range of the thrust is 290 N and the torque is 10 Nm. The resolution of the thrust is 1/8 N and the torque is 1/376 Nm. The sampling rate was 10 KHz.

B. Experimental results and validations

The rotor rotation speed of the experiment varied from 2000 RPM to 8000 RPM with step of 1000RPM and three tests were performed for each rotation speed. CFD simulations were also carried out at the same conditions. The typical velocity distribution was presented in Fig.8. The experimental results were shown in Fig.9. The CFD simulation results were compared with the experimental data and it was found that the simulation results matched the experimental data well, the overestimated thrust might due to the absence of the supporting structures in the duct.

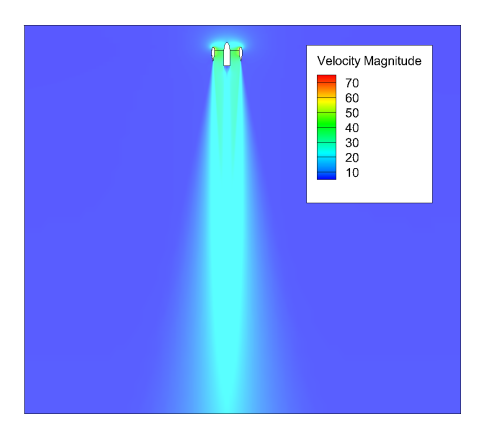


Fig. 8 Velocity distribution of experimental ducted fans flow field

The hovering efficiency of a ducted fan is denoted as the general FM defined in [19]. Its formulations were shown in Eq.7-Eq.9. At the same disk loading (DL), a larger FM means a higher power loading (PL), namely a more efficient ducted fan.

$$FM = PL \cdot \sqrt{\frac{DL}{4\rho}} \tag{7}$$

$$DL = \frac{T_{prop} + T_{duct}}{A} = \frac{T_{total}}{A}$$
 (8)

$$PL = \frac{T_{prop} + T_{duct}}{T_{prop}} = \frac{T_{total}}{P_{prop}}$$
(9)

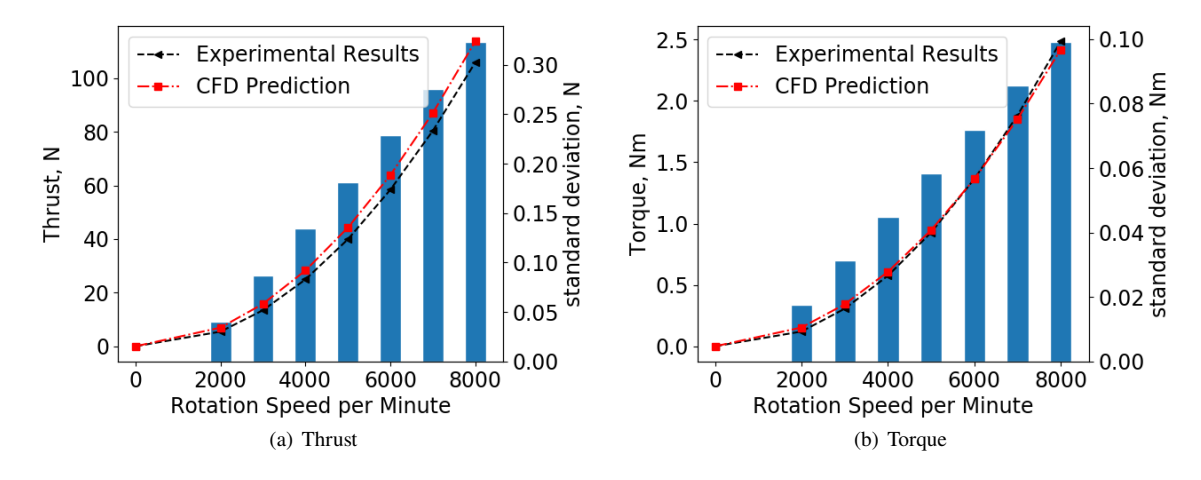


Fig. 9 Comparisons of experiments and CFD prediction

The FM vs. DL was presented in Fig.10. The FM obtained by experiments does not vary too much with DL. The FM predicted by CFD shows the same trend as the experiments, while it overestimated the FM to some extent.

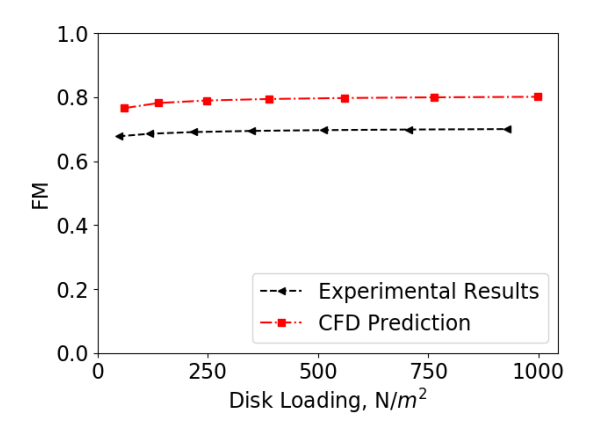


Fig. 10 Figure of Merit comparisons of experiments and CFD prediction

V. Optimization Problem Formulations

A. Objective Functions

In previous ducted propeller optimization studies, the ducted fan thrust was preferred to kept at a fixed value so an equality constraint was introduced. This result in a higher PL at fixed DL which means that a ducted fan with better efficiency was found. However, the SBO cannot enforce the equality constraint well with limited amount of function calls, a fairly loose feasibility tolerance shall be assumed for equality constraints [20], which is not preferred in this study.

As an alternative approach, the FM of the ducted fan was maximized such that the T_{total} is no less than the baseline design in this paper. Since in Fig.10 that the FM varies a little with the DL for a given configuration, the design with higher FM still have higher PL than the one with lower FM if their DL were set to be the same. While this made the optimization easier to be performed as the equality constraint had been removed.

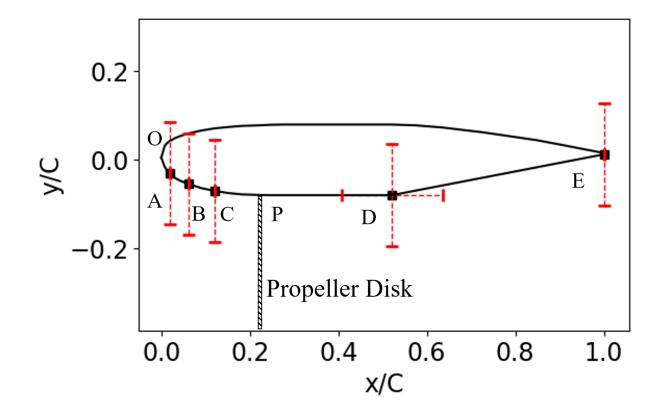


Fig. 11 duct shape control points and deformation direction schematic

B. Design Variables

To investigate the interactions of duct shape and propeller geometries on the performance of the ducted fan, two sets of, with a total number of 16, design variables were chosen to model propeller and duct shapes respectively. Since most of the forces was produced by the inner duct surface [19], subset of the control points near the inner surface were selected to morph the duct. The coordinates of these control points were selected as the design variables.

The six pairs of duct design variables were illustrated in Fig.11. The moving directions of the control points were denoted by the red dashed lines. The inlet radius was controlled by point pair A,B,C and the diffuser length was controlled by point pair D and E. The grids representing the propeller disk were parametrized in a separate FFD volume (Fig.4) so that their shape will not be affected by the deformation, thus the propeller radius remained fixed in all cases.

C. Constraints

Since the Kriging based SBO tends to search the whole design space to find an optimum, any weakness in problem formulation, design space and numerical method will result in an infeasible design. Hence the constraints must be considered carefully. However, if the constraints become too strict, the optimization will lose generalization. In this study, we consider the thrust of the ducted fan as the constraint and penalty function method was adopted to convert the constrained optimization into unconstrained one.

D. Optimization Framework

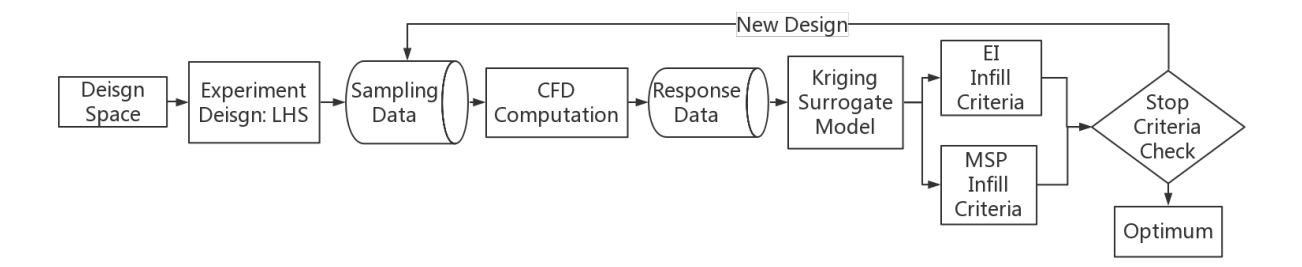


Fig. 12 Framework of the surrogate based optimization

As shown in Fig.12, the initial surrogate model was built by data provided from LHS sampling strategy. Then a sequential optimization was carried out until stop criteria was met. The stop criterion is the maximum iteration count, i.e. if the iteration number exceeded 600, the optimization will be terminated.

VI. Results and discussion

A. Optimization results

In order to explore the benefits from the integrated rotor-duct optimization, three different optimization configurations were studied. Their optima were compared with the case of baseline duct and baseline propeller (BDBP). The baseline duct (BD) was the same as the one validated in experiments. The baseline propeller (BP) was originated from the experiment propeller but has an 8 degree increase of twist angle for larger thrust. All cases shared the same rotor diameter. It was expected that the results from these cases could help us to understand how the formulation of the optimization model could affect the hover efficiency of the ducted fan. The definition of each configuration is as follows:

- 1. BDOP model: Baseline duct, optimized propeller, i.e. the propeller was optimized based on the baseline duct.
- 2. ODBP model: Optimized duct, baseline propeller, i.e. the duct shape was optimized with the baseline propeller.
- 3. IO model: Integrated optimization, i.e. both the propeller and duct shape were involved in the optimization.

The optimizations were performed on a workstation which has two eight-core 3.4GHz Intel Xeon E5-2687w processors, with the total RAM of 128 GB. The time for each case was about 80h, the convergence histories of these cases are shown in Fig.13.

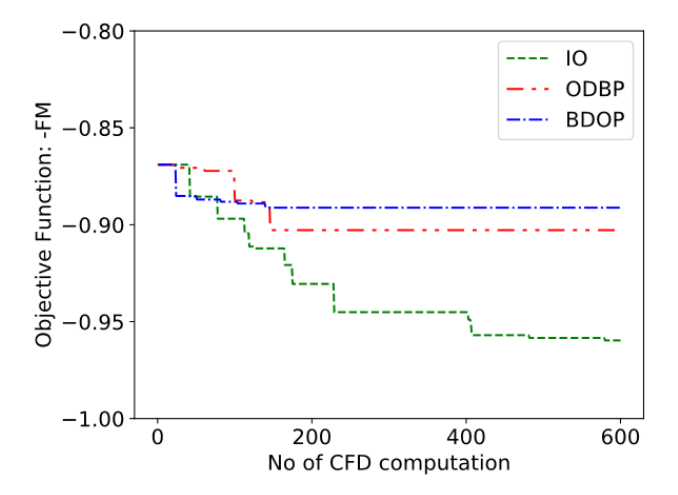


Fig. 13 Convergence history of the optimizations

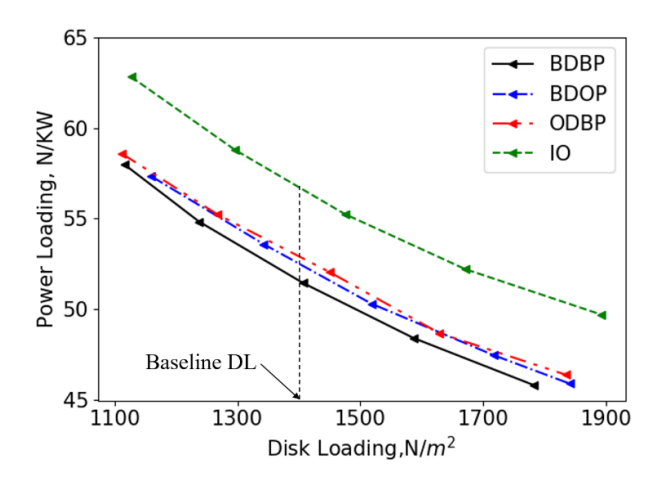


Fig. 14 Comparison of the hover efficiency

The performances of the optimized ducted fan systems were compared by PL vs. DL curve, as illustrated in Fig.14. It can be seen that both the BDOP and ODBP tend to perform better than the baseline design, while the IO is significantly superior to the other two configurations.

B. Crossover studies

Table 2 Crossover cases

Duct	Rotors	BP	OP	IOP
BD		BDBP	BDOP	BD+IOP
OD		ODBP	OD+OP	OD+IOP
IOD		IOD+BP	IOD+OP	IO

To investigate the effectiveness of the integrated rotor-duct shape optimization, several crossover studies of the optimized ducted fans were conducted. The optimized propellers and ducts were swapped among these cases. The T_{total} was kept the same as BDBP. This results in a constant DL for all cases to be discussed. Shown in Table 2, the crossover of these four cases resulted in five new cases described below, and the performances of these cases are presented in Table 3.

- 1. OD+OP: optimized duct of ODBP with the optimized propeller of BDOP.
- 2. BD+IOP: baseline duct with the optimized propeller of IO.
- 3. OD+IOP: optimized duct of ODBP with the optimized propeller of IO.
- 4. IOD+BP: optimized duct of IO with the baseline propeller.
- 5. IOD+OP: optimized duct of IO (IOD) with the optimized propeller of BDOP

PL Rotor Thrust **Duct Thrust** DL Ducted fans **RPM** FM N/m^2 N/KW N N **BDBP** 8000 65.720 94.378 1404.262 51.340 0.86910 **ODBP** 7874 1402.464 53.394 0.90326 60.259 99.634 **BDOP** 7691 62.950 96.977 1402.757 52.316 0.88516 IO 7802 53.988 106.103 1404.197 56.632 0.95855 OD+OP 7851 102.505 54.453 0.92140 57.470 1403.171 **BD+IOP** 7807 62.014 97.862 1402.321 52.225 0.88318 103.827 OD+IOP 7709 56.055 1402.373 54.657 0.92490 IOD+BP 9325 102.014 56.078 34.481 0.59070 1386.662 IOD+OP 7772 55.778 104.061 1401.979 55.951 0.94611

Table 3 Performance of crossover ducted fans

The design spaces for the three different optimization configurations are illustrated in Fig.15. For optimization that only the duct shape is involved, the design space is denoted by red plane. While for only propeller shape is considered the design space is represented by the green plane. When these two sets design variables are simultaneously considered, the design space is extended as the light purple cube.

The ODBP performs much better than the IOD+BP and the BDOP performs better than the BD+IOP as well. Since IOD+BP and ODBP is in the same design space, i.e., they are in the same red plane, and the design space for BD+IOP and BDOP are also the same, this may prove that the ODBP and BDOP has reached a relative optimal duct system in their own design space. Fig.15 highlight the superiority of IO from mathematical perspective as that with the combination of these two sets design variables, optimal duct configurations will be introduced in the new design space.

Meanwhile, it can be seen that the OD+OP is better than ODBP and BDOP, one may conclude that optimizing duct and propeller separately might also benefit the system. However, IO obviously outperforms the OD+OP, this comparison has verified the effectiveness of IO and also shown the coupling effect between the propellers and the duct as IO and OD+OP are basically two different configuration in the design space.

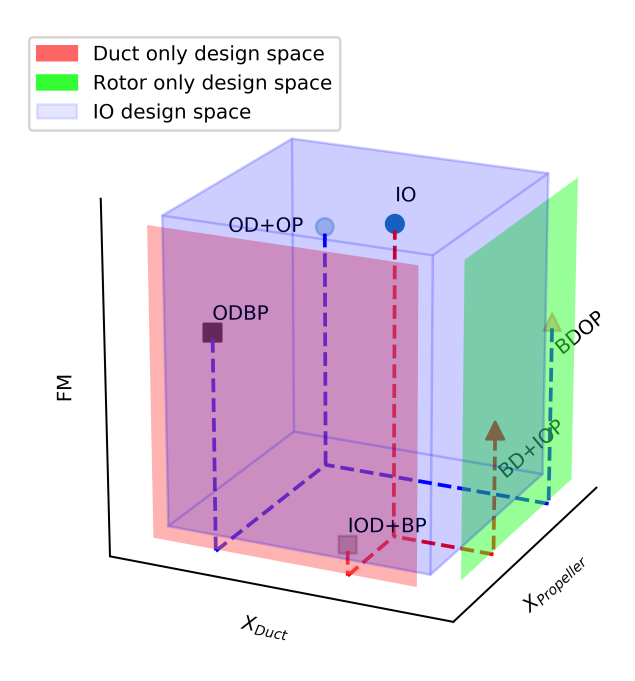


Fig. 15 Design space for different design variables

The thrust of ducted fans vs FM was illustrated in Fig.16. The T_{total} for all cases roughly equals 160 N. It can be seen the more efficient the ducted fan the more portion of thrust will tend be produced by the duct.

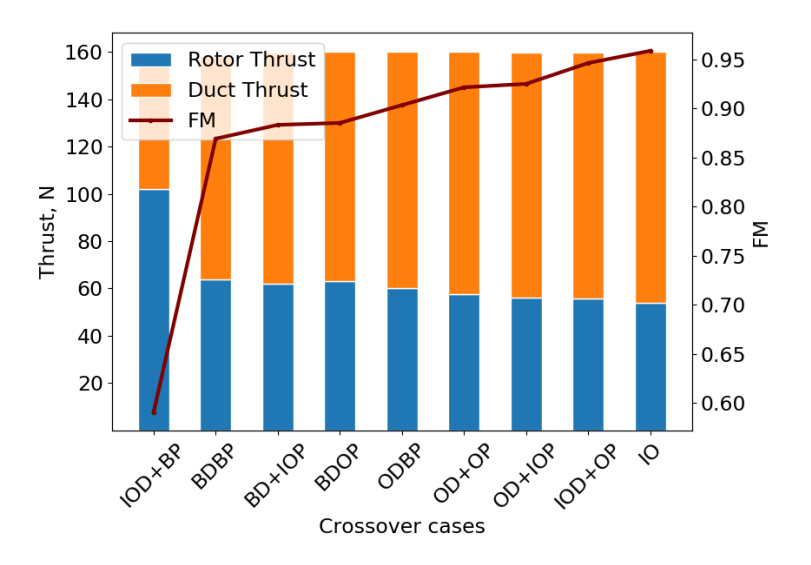


Fig. 16 Thrust and FM compare of different crossover cases with the same T_{total}

C. Effects of the duct shape

The optimized duct shapes of ODBP and IO are presented in Fig.17. In comparison with the baseline design BDBP, the optimization tends to result in larger duct inlet radius and larger diffuser length and expansion angle. The results of the IO have the largest inlet radius and diffuser expansion angle.

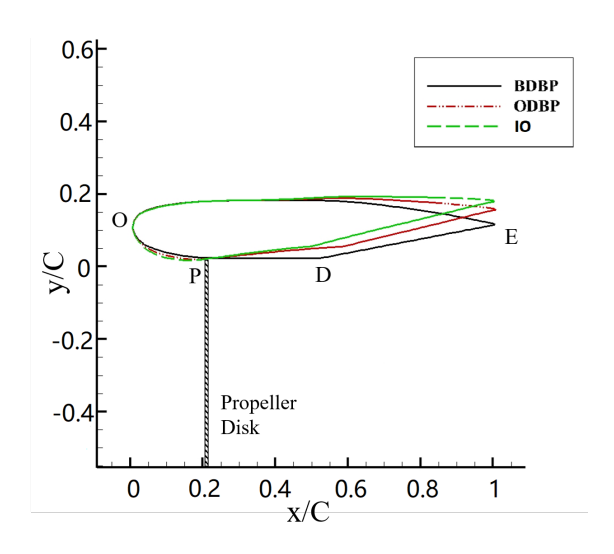


Fig. 17 Duct Shape optimization results

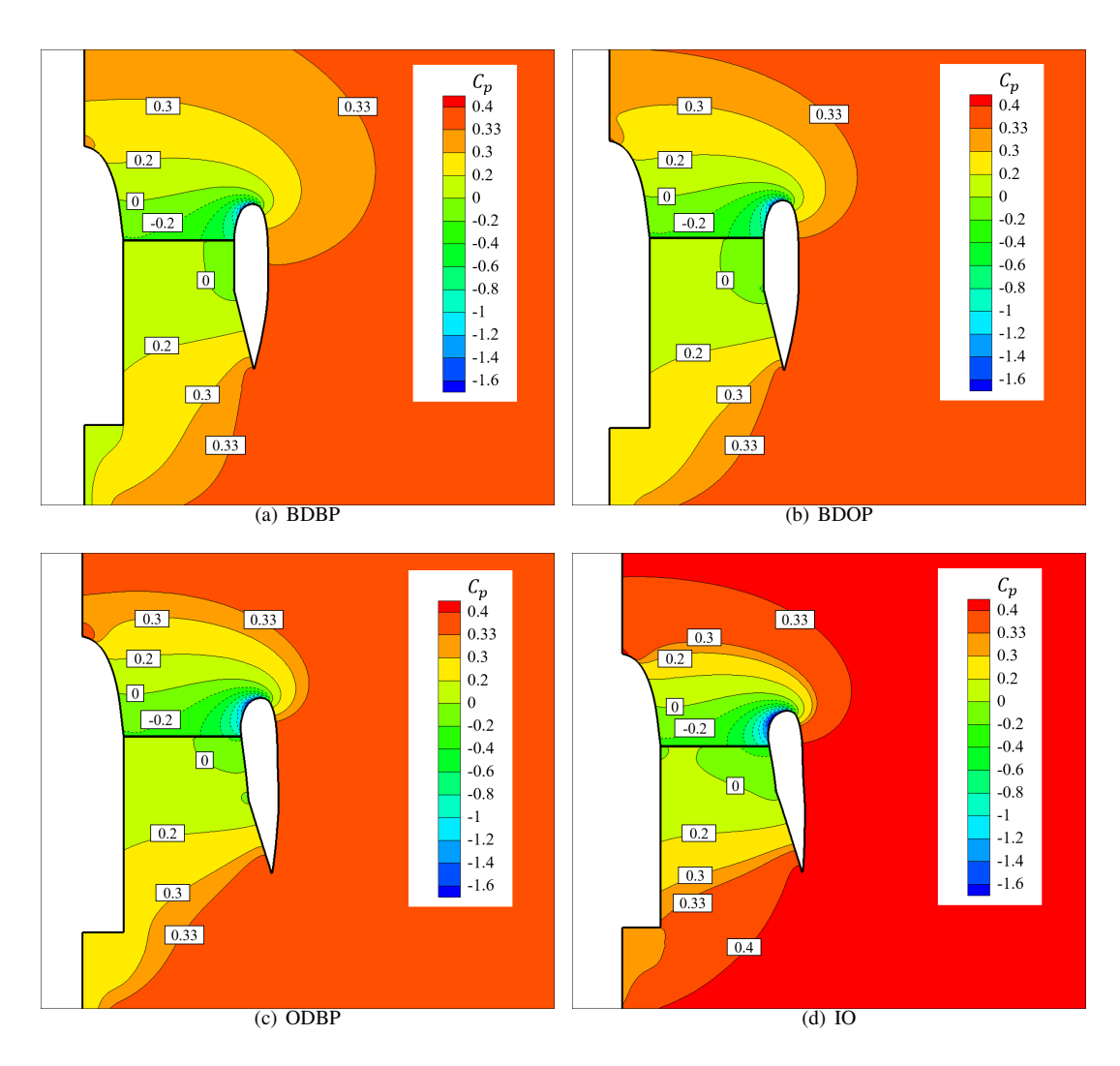


Fig. 18 Flow field of the ducted fans: (a) BDBP, (b) BDOP, (c) ODBP, (d) IO

The C_p distribution of the three optimization cases and the baseline design were provided in Fig.18. The pressure coefficient used in the figure was defined in Eq.10. Negative pressure coefficient contour was denoted by dashed lines. It can be seen that for all cases there is a high speed region that results in negative pressure coefficient, or the lip suction thrust, near the duct inlet lips. Below the propeller disk, flow speed decreases and the pressure coefficient rises, the increased static pressure tend to push the duct diffusion segment upwards. The duct's thrust, which can be derived from the pressure distributions along the duct, are primarily originated from the lip suction thrust and diffuser thrust.

$$C_p = \frac{P - P_{\infty}}{q_{a_{tip_{baseline}}}} = \frac{2(P - P_{\infty})}{\rho V_{a_{tip_{baseline}}}^2}$$
(10)

The pressure coefficient along the ducts was shown in Fig.19. The design with higher efficiency tends to have larger lip radius (Fig.18) and lower C_p at the lip. As the ODBP(Fig.18(c)) and IO(Fig.18(d)) cases resulted in larger diffuser expansion angles, there is higher static pressure in the diffuser. Higher static pressure along with larger expansion angle can increase the axial force component due to pressure, which introduces larger diffuser thrust.

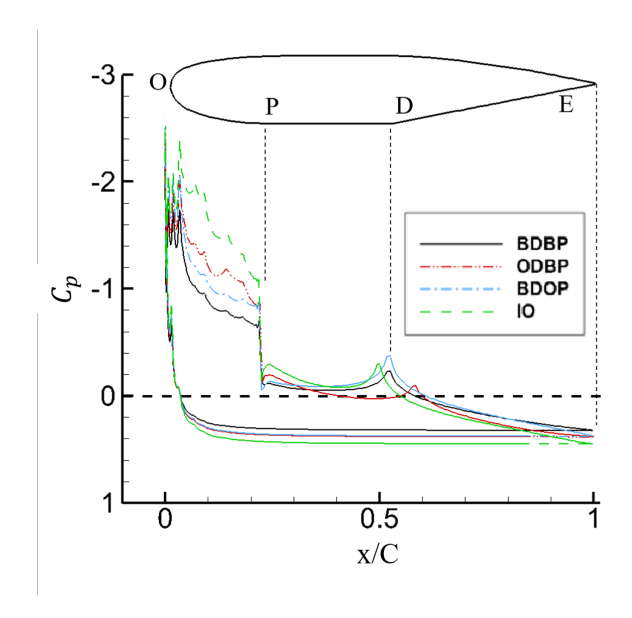


Fig. 19 Pressure coefficient around the duct

The axial speed contour of IOD+BP was presented in Fig.20(a), with the IO case as a reference (Fig.20(b)). The IOD+BP case draws attention for its dramatically decreased efficiency. The difference of IO and IOD+BP is the propeller. In the IOD+BP case, as shown in fig.18a, flow separation starts from the region just above the propeller to all parts of the diffuser. To improve the hovering efficiency of the ducted fan, larger diffuser expansion angle is preferred. However, the maximum diffuser expansion angle is constrained by the flow separation. In Fig.20(a), it can be seen that the IO can help to prevent flow separation at large diffuser expansion angle.

D. Effects of the propeller geometry

The optimized propeller geometries are presented in Fig.21, the red dotted vertical line represents the design space of each design variable. It can be seen that the chord at the tip is longer than that at the middle part of the blade. The rotor in the duct can be deemed as a flow control device that utilizes the mass blowing to control the boundary layer of the inner duct wall. As shown in Eq.11, longer chord length at the blade tip injects more momentum and kinetic energy into the flow and results in higher velocity near the duct wall (Fig.20-Fig.22). The boundary layer separations can be delayed by the air stream of increased velocity as the boundary layer friction deceleration is reversed. These results can also serve as a proof for the declaration by Jimenez [21] who claimed that the outboard biased inflow distribution, here shown in Fig.22, may result in a more efficient ducted rotor system for hovering performance.

$$S_{M_Z} = N_p \frac{\rho v^2 c (C_l cos\beta - C_d sin\beta)}{4\pi r}$$
 (11)

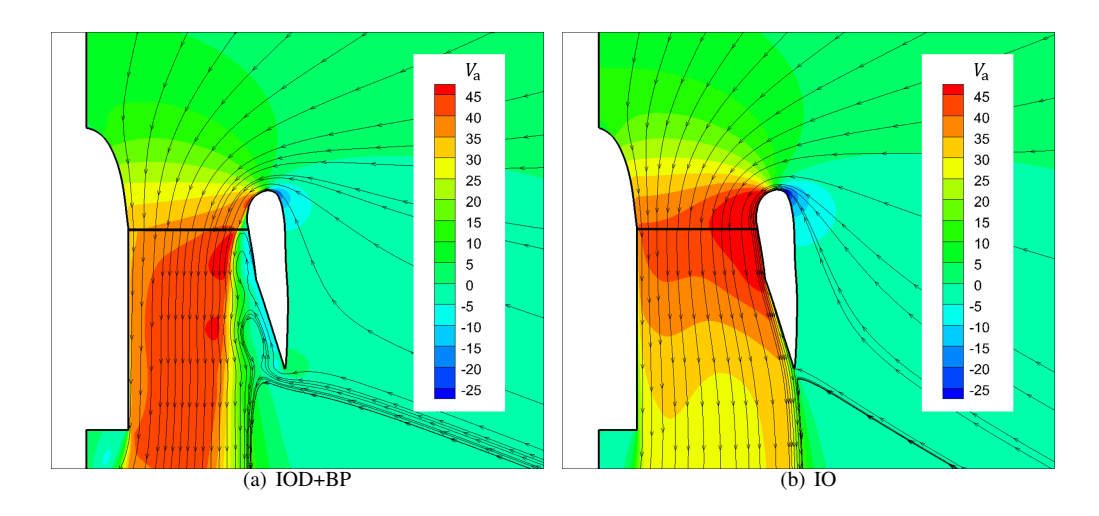


Fig. 20 Flow field comparison of (a) IOD+BP and (b) IO

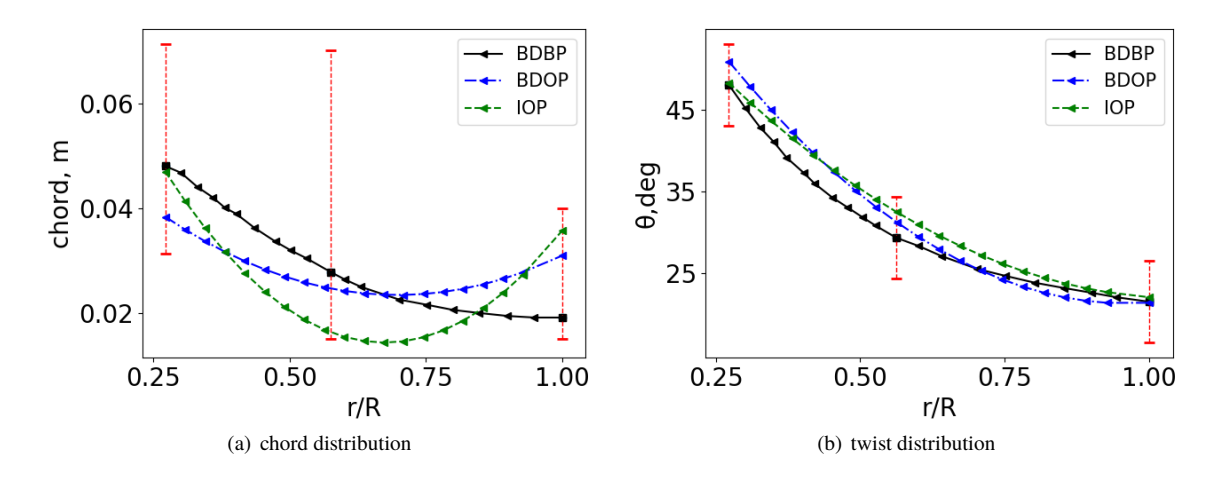


Fig. 21 propeller chord and twist angle distribution along the radius

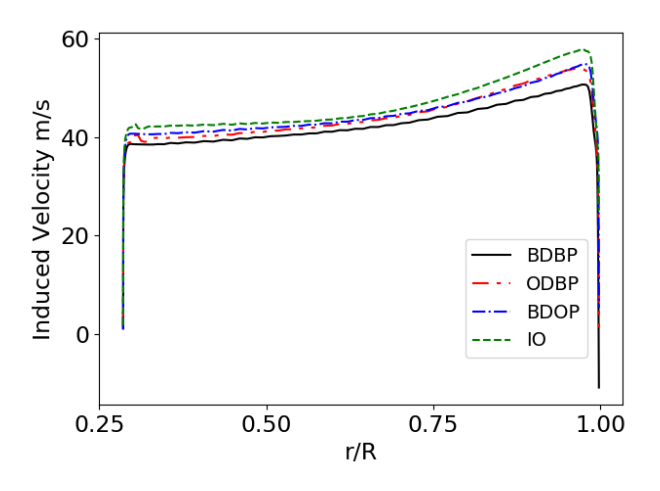


Fig. 22 Induced velocity comparison of different ducted fans

VII. Conclusions

In this paper, the hovering performance of the ducted fan was analyzed by the RANS along with the MSM. The experiment has been conducted and the CFD prediction matched experiment data well. An integrated rotor-duct optimization was then performed with the help of Kriging surrogate based optimization, and crossover studies were carried out. Several conclusions can be drawn base on the preceding analysis:

- 1. The propeller optimization within a duct is different from an open propeller, an outboard-biased blade distribution and velocity distribution is found for a more efficient design.
- 2. For a more efficient ducted fan, more part of the thrust will be produced by the duct. The approaches to enlarge the duct thrust are increasing inlet radius and expansion angle of the diffuser. However, the improvement of the hovering efficiency is primarily restricted by the flow separations in the duct.
- 3. The integrated rotor-duct optimization can find a better design with delayed flow separation. When the interactions of the rotor and duct were considered, there will be longer chord length at the blade tip. This will inject more momentum into the boundary layer of the inner duct wall and helps keeping the flow attached.

References

- [1] Grunwald, K. J., and Goodson, K. W., "Aerodynamic loads on an isolated shrouded-propeller configuration for angles of attack from -10 degrees to 110 degrees," Tech. rep., National Aeronautics and space administration Washington DC, 1962.
- [2] Black, D., and ROHRBACH, C., "Shrouded propellers-a comprehensive performance study," 5th Annual Meeting and Technical Display, 1968, p. 994.
- [3] Mort, K. W., "Performance characteristics of a 4-foot-diameter ducted fan at zero angle of attack for several fan blade angles," 1965
- [4] Graf, W., Fleming, J., and Ng, W., "Improving ducted fan uav aerodynamics in forward flight," 46th AIAA Aerospace Sciences Meeting and Exhibit, 2008, p. 430.
- [5] Yilmaz, S., Erdem, D., and Kavsaoglu, M., "Performance of a ducted propeller designed for UAV applications at zero angle of attack flight: an experimental study," *Aerospace Science and Technology*, Vol. 45, 2015, pp. 376–386.
- [6] Ahn, J., and Lee, K., "Performance prediction and design of a ducted fan system," 40th AIAA/ASME/SAE/ASEE Joint Propulsion Conference and Exhibit, 2004, p. 4196.
- [7] Schaller, D. F., "A technique for shape optimization of ducted fans," 2007.
- [8] Chang, I.-C., and Rajagopalan, R., "CFD analysis for ducted fans with validation," 21st AIAA Applied Aerodynamics Conference, 2003, p. 4079.
- [9] Akturk, A., and Camci, C., "A computational and experimental analysis of a ducted fan used in VTOL UAV systems," Department of Aerospace Engineering, Pennsylvania University, USA, 2011.
- [10] Lakshminarayan, V. K., and Baeder, J. D., "Computational investigation of microscale shrouded rotor aerodynamics in hover," *Journal of the American Helicopter Society*, Vol. 56, No. 4, 2011, pp. 1–15.
- [11] Rajagopalan, R. G., and Mathur, S. R., "Three dimensional analysis of a rotor in forward flight," *Journal of the American Helicopter Society*, Vol. 38, No. 3, 1993, pp. 14–25.
- [12] Drela, M., "XFOIL: An analysis and design system for low Reynolds number airfoils," *Low Reynolds number aerodynamics*, Springer, 1989, pp. 1–12.
- [13] Nygaard, T. A., Dimanlig, A. C., and Meadowcroft, E. T., "Application of a momentum source model to the RAH-66 Comanche FANTAIL," 2004.
- [14] Goldberg, D. E., and Holland, J. H., "Genetic algorithms and machine learning," *Machine learning*, Vol. 3, No. 2, 1988, pp. 95–99.
- [15] Skinner, S. N., and Zare-Behtash, H., "State-of-the-art in aerodynamic shape optimisation methods," *Applied Soft Computing*, 2017.
- [16] Han, Z.-H., Zhang, Y., Song, C.-X., and Zhang, K.-S., "Weighted gradient-enhanced kriging for high-dimensional surrogate modeling and design optimization," AIAA Journal, 2017, pp. 4330–4346.
- [17] McKay, M. D., Beckman, R. J., and Conover, W. J., "Comparison of three methods for selecting values of input variables in the analysis of output from a computer code," *Technometrics*, Vol. 21, No. 2, 1979, pp. 239–245.
- [18] Couckuyt, I., Dhaene, T., and Demeester, P., "ooDACE toolbox: a flexible object-oriented Kriging implementation," *The Journal of Machine Learning Research*, Vol. 15, No. 1, 2014, pp. 3183–3186.
- [19] Pereira, J. L., "Hover and wind-tunnel testing of shrouded rotors for improved micro air vehicle design," Tech. rep., Maryland Univ College Park Dept of Aerospace Engineering, 2008.
- [20] Audet, C., Denni, J., Moore, D., Booker, A., and Frank, P., "A surrogate-model-based method for constrained optimization," 8th Symposium on Multidisciplinary Analysis and Optimization, 2000, p. 4891.
- [21] Jimenez, B. G., and Singh, R., "Effect of duct-rotor aerodynamic interactions on blade design for hover and axial flight," *53rd AIAA Aerospace Sciences Meeting*, 2015, p. 1030.